Multireference Frame Based Open-Phase Fault Modeling and Control for Asymmetrical Six-Phase Interior Permanent Magnet Motors

Wenlong Li, *Senior Member, IEEE*, Guodong Feng, *Senior Member, IEEE*, Ze Li, *Student Member, IEEE*, Jimi Tjong, and Narayan C. Kar, *Senior Member, IEEE*

***Abstract*—Multireference frame based asymmetric six-phase interior permanent magnet motor modeling and control strategy under single open-phase fault are investigated in this article. The motor modeling under healthy operation is firstly established based on a dual *dq*-axis synchronous rotating frame. With this dual *dq*-axis frame, the motor modeling considering the magnetic saturation effect under open-phase fault has been derived. By introducing a dual-direction rotating frame, the stator current under single open-phase fault can be treated as the sum of a positive current sequence and a negative current sequence. With this dual-direction rotating frame, the two current sequences can be transformed into two dc components for fault-tolerant operation. Fault-tolerant control schemes with maximum torque per ampere for copper loss minimization and torque maximization are developed, respectively. Finally, the validity of the proposed modeling and control are evaluated by experiments under both steady and transient scenarios.**

***Index Terms*—Asymmetrical six-phase, fault-tolerant control, interior permanent magnet motor (IPMM), maximum torque per ampere (MTPA), multireference frame, open-phase fault.**

I. Introduction

ASYMMETRICAL six-phase permanent-magnet (PM) motors have higher power density, efficiency, fault-tolerant capability, and lower torque ripple, compared to three-phase counterparts and attracts more and more attention recently [1]–[4]. This kind of motors, as known as the dual three-phase motor, has two groups of three-phase winding which can be connected to a single or two separate neutral points. Since they possess two separate three–phase winding groups, the motors can be supplied from two separate inverters with reduced power rating. It also alleviates the electrical stress and thermal dissipation in power devices and with a reduced size. Moreover, due to the multiphase configuration the reliability and fault-tolerant capability improved greatly [5]–[8].

The modeling and control of six-phase motors can be categorized into two groups, namely the vector space decomposition (VSD) approach and the modeling based on two synchronous rotating frames [9]. The VSD modeling is applied for suppressing the harmonics caused by the inverter switching operation [10]. It projects the six-phase winding into three orthogonal subspaces, namely $\alpha\beta$ plane (torque-producing plane), *xy* plane (nontorque-producing plane), and $0_1 0_2$ plane (zero-sequence plane). Then, by using stationary to rotating frame transformation, two *dq*–axes are established in $\alpha\beta$ plane and *xy* plane, respectively [11], [12]. The other approach is to treat the two winding group separately, and transformed into rotating frames one by one to form another dual *dq*-axis. The other is the dual synchronous rotating frame control which is obtained by directly using the Park–Clarke transformation to each set of the three-phase winding [13]. Based on this approach, two sets of the three-phase winding are modeled into two *dq*–axes which can be regarded as the extended modeling of the traditional three-phase motors. Since the two *dq*-axes are generally mutually coupled with each other due to the motor magnetic structure, an approach is proposed to diagonalize the transformed inductance matrix based on the dual *dq*-axis for eliminating the mutual coupling. Consequently, the new dual *dq*-axis based models are identical with those dual *dq*-axis transformed for the $\alpha\beta$ plane and *xy* plane from the VSD transformation.

The multiphase motors are usually claimed for the high capability in fault-tolerant operations [14]–[22]. Stator phase failure, such as open-phase fault, is one typical fault of the multiphase motors. Recently, various research studies have been conducted on open-phase fault modeling and control for six-phase motors. A fault-tolerant direct torque control scheme was proposed for a six-phase permanent magnet synchronous motor (PMSM) with a single neutral point [17]. With this control strategy, a fast and smooth torque response can be achieved with any two phases opened. A fault-tolerant control (FTC) scheme was proposed for a six-phase induction motor not only to realize a ripple-free operation but also to enhance the braking process after an open-circuit fault, with injection of circulating currents [18]. An optimal FTC for a six-phase induction motor drive

Manuscript received December 11, 2020; revised March 3, 2021; accepted March 27, 2021. Date of publication April 13, 2021; date of current version June 30, 2021. Recommended for publication by Associate Editor J. Ye. *(Corresponding author: Wenlong Li.)*

Wenlong Li was with the Department of Electrical and Computer Engineering, University of Windsor, Windsor, ON N9B 3P4, Canada. He is now with the School of Automation, Nanjing University of Science and Technology, Nanjing 210094, China (e-mail: liwl.ustc@hotmail.com).

Ze Li, Jimi Tjong, and Narayan C. Kar are with the Department of Electrical and Computer Engineering, University of Windsor, Windsor, ON N9B 3P4, Canada (e-mail: li111169@uwindsor.ca; jimi.tjong@uwindsor.ca; nkar@uwindsor.ca).

Guodong Feng is with the School of Intelligent Systems Engineering, Sun Yat-sen University, Guangzhou 510275, China (e-mail: qqfengguodong@gmail.com).

Color versions of one or more figures in this article are available at https://doi.org/10.1109/TPEL.2021.3072947.

Digital Object Identifier 10.1109/TPEL.2021.3072947

using two parallel converters was presented [19]. Up to three faults for configurations of single and two neutral points have been investigated aiming at optimizing the postfault current and smooth transition from healthy to faulty operation. A fault-tolerant control based on two synchronous rotating frames for surface-mounted dual PMSM was presented and studied [20]. Two different FTC modes for minimizing copper loss and maximizing output torque after open-phase fault have been proposed and verified. However, the control scheme is applied for the surface-mounted PMSM with two neutral points only and cannot deal with the motors having interior PMs. An open-phase fault modeling and control for dual three-phase PMSM two neutral points was proposed based on VSD [21]. Using this model, the stator currents can be optimized by genetic algorithm to maximize the output torque and minimize the torque ripple. Although this control strategy is feasible and can be applied for both surface-mounted and interior PMs, the modeling and FTC based on VSD has little physical insight on the relationship between the two winding groups and cannot operate when more than one phase are at fault.

The power switches are vulnerable and it is reported that 38% of the motor drive faults are caused by the power switch failures [22]. When this fault occurs, the machine phases will be opened [20], [21]. The objective of this article is to develop an open-phase fault model and control strategy for asymmetrical six-phase interior permanent magnet motors (IPMMs) postfault operation based on multireference frames. By using this model, the two winding groups of this IPMM, namely phases *abc* and *xyz*, can be treated separately and the motor can perform a ripple-free operation with more than one phase opened from the same winding group. Then, by introducing the dual-direction rotating reference frame, currents flowing in the stator after one phase opened can be represented as sums of a positive current sequence and a negative current sequence. By considering overcurrent protection and maximum torque per ampere (MTPA) control, the optimized current amplitudes and angles for both winding groups are achieved for copper loss minimization and torque maximization, respectively. Finally, the proposed modeling and FTC schemes are verified by the experimental results under different operating scenarios.

II. Dual DQ-Axis Based Healthy Motor Model

Since the asymmetrical six-phase IPMMs are featured by the rotor saliency, the inductance is a function of the rotor position θ, which can be represented into the sum of a dc component $\mathbf{L_{st}}$ and a fundamental component $\mathbf{L_{sa}}$. Therefore, the phase inductance can be expressed as

$$\mathbf{L} = \mathbf{L_{st}} - \mathbf{L_{sa}}(\theta). \tag{1}$$

The dc component is given by

$$\mathbf{L_{st}} = \begin{bmatrix} \mathbf{L_{11}} & \mathbf{M_{12}} \\ \mathbf{M_{21}} & \mathbf{L_{22}} \end{bmatrix} + \mathrm{diag}(L_{al}, L_{al}, L_{al}, L_{al}, L_{al}, L_{al}) \tag{2}$$

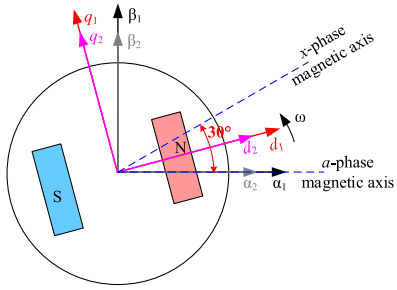

Fig. 1. Dual dq-axis for the asymmetrical six-phase IPMM.

$$\mathbf{L_{11}} = \mathbf{L_{22}} = \frac{L_0}{2}\begin{bmatrix} 2 & -1 & -1 \\ -1 & 2 & -1 \\ -1 & -1 & 2 \end{bmatrix},$$

$$\mathbf{M_{12}} = \mathbf{M_{21}^{T}} = \frac{\sqrt{3}L_0}{2}\begin{bmatrix} 1 & -1 & 0 \\ 0 & 1 & -1 \\ -1 & 0 & 1 \end{bmatrix},$$

where L_0 and L_{al} are static component and leakage inductance, respectively.

The phase-shift of $\pi/6$ is one of the most popular dual three-phase motor configurations. In fact, different phase-shift can result in significant differences in the electromagnetic performances. The phase-shift of $\pi/6$ configuration has a larger torque density and a lower torque ripple, and under the three-phase open-circuit condition the unbalanced magnetic force does not exist for the $\pi/6$ phase-shift configuration [2]. For a phase-shift of $\pi/6$, the position-dependent fundamental inductance is given by

$$\mathbf{L_{sa}}(\theta) = L_{\Delta}\begin{bmatrix} \mathbf{\Theta_{11}} & \mathbf{\Theta_{12}} \\ \mathbf{\Theta_{21}} & \mathbf{\Theta_{22}} \end{bmatrix} \tag{3}$$

where $\mathbf{\Theta_{11}} = \mathbf{\Theta}(\theta)$

$$= \begin{bmatrix} \cos 2\theta & \cos(2\theta - 2\pi/3) & \cos(2\theta + 2\pi/3) \\ \cos(2\theta - 2\pi/3) & \cos(2\theta + 2\pi/3) & \cos 2\theta \\ \cos(2\theta + 2\pi/3) & \cos 2\theta & \cos(2\theta - 2\pi/3) \end{bmatrix},$$

$\mathbf{\Theta_{22}} = \mathbf{\Theta}(\theta - \pi/6)$

$$= \begin{bmatrix} \cos(2\theta - \pi/3) & -\cos(2\theta) & \cos(2\theta + \pi/3) \\ -\cos(2\theta) & \cos(2\theta + \pi/3) & \cos(2\theta - \pi/3) \\ \cos(2\theta + \pi/3) & \cos(2\theta - \pi/3) & -\cos(2\theta) \end{bmatrix}$$

$$\mathbf{\Theta_{12}} = \mathbf{\Theta_{21}} = \mathbf{\Theta}(\theta - \pi/12)$$

$$= \begin{bmatrix} \cos(2\theta - \pi/6) & \cos(2\theta - 5\pi/6) & -\sin(2\theta) \\ \cos(2\theta - 5\pi/6) & -\sin(2\theta) & \cos(2\theta - \pi/6) \\ -\sin(2\theta) & \cos(2\theta - \pi/6) & \cos(2\theta - 5\pi/6) \end{bmatrix}, \text{ and}$$

L_{Δ} is the amplitude of the position-dependent inductance.

Fig. 1 shows the relationship based on two synchronous rotating frames, namely $d1q1$- and $d2q2$-axis. Although two groups of the three-phase winding have a phase-shift of $\pi/6$, the two dq-axes are kept in phase. Here, $d1q1$-axis is applied for modeling of the winding group phase *abc*, and $d2q2$-axis is applied for modeling of the winding group phase *xyz*. The two groups of three-phase winding *abc* and *xyz* are firstly projected to $\alpha1\beta1$-axis and $\alpha2\beta2$-axis using (4), where the $\alpha1$-axis and $\alpha2$-axis align with the *a*-phase magnetic axis. Then, they are transformed to $d1q1$-axis and $d2q2$-axis using (5). Hence, the

dual dq-axis based asymmetrical six-phase motor modeling is achieved.

$$\mathbf{T}_{\alpha\mathbf{1}\beta\mathbf{1}}=\frac{1}{3}\begin{bmatrix}2&-1&-1\\0&\sqrt{3}&-\sqrt{3}\\1&1&1\end{bmatrix},\mathbf{T}_{\alpha\mathbf{2}\beta\mathbf{2}}=\frac{1}{3}\begin{bmatrix}\sqrt{3}&-\sqrt{3}&0\\1&1&-2\\1&1&1\end{bmatrix} \tag{4}$$

$$\mathbf{T_{dq}}=\begin{bmatrix}\cos\theta&\sin\theta&0\\-\sin\theta&\cos\theta&0\\0&0&1\end{bmatrix}. \tag{5}$$

The inductance matrix for two winding groups can be transformed to the dual dq-axis by (6) and (7) shown at bottom of this page.

From (6) and (7), the inductance matrices after transformation are shown as follows:

$$\mathbf{L_{d1q1}}=\mathbf{L_{d2q2}}=\frac{3}{2}\begin{bmatrix}L_0-L_\Delta&0&0\\0&L_0+L_\Delta&0\\0&0&0\end{bmatrix}+L_{al}\begin{bmatrix}1&0&0\\0&1&0\\0&0&1\end{bmatrix} \tag{8}$$

$$\mathbf{M_{dq12}}=\mathbf{M_{dq21}}=\frac{3}{2}\begin{bmatrix}L_0-L_\Delta&0&0\\0&L_0+L_\Delta&0\\0&0&0\end{bmatrix}. \tag{9}$$

The $d1q1$-axis flux linkage for the winding group phase abc is given by

$$\begin{cases}\lambda_{d1}=L_{d1}i_{d1}+M_{d1d2}i_{d2}+\psi_{PM}\\ \lambda_{q1}=L_{q1}i_{q1}+M_{q1q2}i_{q2}\end{cases} \tag{10}$$

where $L_{d1}, L_{q1}, M_{d1\,d2}, M_{q1\,q2}$, and ψ_{PM} are $d1$-axis inductance, $q1$-axis inductance, mutual inductances between $d1$ and $d2$ axes, between $q1$ and $q2$ axes, and the PM flux linkage, respectively.

The torque component produced by phase abc can be calculated by the cross product of its flux and current

$$\begin{aligned}T_{e1}&=\frac{3}{2}P(\lambda_{d1}i_{q1}-\lambda_{q1}i_{d1})=\frac{3}{2}P[\psi_{PM}i_{q1}\\&\quad+(L_{d1}-L_{q1})i_{d1}i_{q1})\\&\quad+\frac{3}{2}P(M_{d1d2}i_{d2}i_{q1}-M_{q1q2}i_{q2}i_{d1}).\end{aligned} \tag{11}$$

From (11), it can be seen that besides the electromagnetic torque component and the reluctance torque components produced by phase abc, and the mutual coupling between two winding groups also contribute torque components which differentiates from the modeling based on VSD transformation.

Similarly, the $d2q2$-axis flux linkages for the winding group phase xyz are given by

$$\begin{cases}\lambda_{d2}=L_{d2}i_{d2}+M_{d1d2}i_{d1}+\psi_{PM}\\ \lambda_{q2}=L_{q2}i_{q2}+M_{q1q2}i_{q1}\end{cases} \tag{12}$$

where L_{d2} and L_{q2} are $d2$-axis and $q2$-axis inductances, respectively.

The torque component produced by phase xyz is obtained by

$$\begin{aligned}T_{e2}&=\frac{3}{2}P(\lambda_{d2}i_{q2}-\lambda_{q2}i_{d2})=\frac{3}{2}P[\psi_{PM}i_{q2}\\&\quad+(L_{d2}-L_{q2})i_{d2}i_{q2}]\\&\quad+\frac{3}{2}P(M_{d1d2}i_{d1}i_{q2}-M_{q1q2}i_{q1}i_{d2}).\end{aligned} \tag{13}$$

Therefore, the resultant torque of the asymmetrical six-phase IPMM is given by

$$T_e=T_{e1}+T_{e2}. \tag{14}$$

According to (11), (13), and (14), the resultant torque can also be expressed into two components, namely the electromagnetic torque component and reluctance torque component, respectively, as in (15) shown at bottom of this page.

Although there are two neutral points and the modeling of two groups of three–phase winding are independent with some mutual couplings. The currents applied to two groups of winding should follow their magnetic geometry. Therefore, current relationship between $d1q1$- and $d2q2$-axis is governed by:

$$I_{d2}=I_{d1},\ I_{q2}=I_{q1} \tag{16}$$

Due to this relationship of currents for the two dq-axes, the torque components produced by winding abc and xyz should be equal at all the time under normal operation, according to (11) and (13).

III. Torque Modeling Under Open-Phase Fault

In this article, the asymmetrical six-phase IPMM under investigation has two isolated neutral points. When more than one phase from the same winding group such as phase abc are opened, the faulty winding group will be isolated and only the health winding group, i.e., phase xyz is engaged for operation. At this situation, the torque developed by the single three-phase

$$\begin{cases}\mathbf{L_{d1q1}}=\mathbf{T_{dq}}\mathbf{T}_{\alpha\mathbf{1}\beta\mathbf{1}}(\mathbf{L_{11}}+diag(L_{al},L_{al},L_{al})-L_\Delta\mathbf{\Theta_{11}})\mathbf{T}^{-1}_{\alpha\mathbf{1}\beta\mathbf{1}}\mathbf{T}^{-1}_{\mathbf{dq}}\\ \mathbf{L_{d2q2}}=\mathbf{T_{dq}}\mathbf{T}_{\alpha\mathbf{2}\beta\mathbf{2}}(\mathbf{L_{22}}+diag(L_{al},L_{al},L_{al})-L_\Delta\mathbf{\Theta_{22}})\mathbf{T}^{-1}_{\alpha\mathbf{2}\beta\mathbf{2}}\mathbf{T}^{-1}_{\mathbf{dq}}\end{cases} \tag{6}$$

$$\begin{cases}\mathbf{M_{dq12}}=\mathbf{T_{dq}}\mathbf{T}_{\alpha\mathbf{1}\beta\mathbf{1}}(\mathbf{M_{12}}-L_\Delta\mathbf{\Theta_{12}})\mathbf{T}^{-1}_{\alpha\mathbf{2}\beta\mathbf{2}}\mathbf{T}^{-1}_{\mathbf{dq}}\\ \mathbf{M_{dq21}}=\mathbf{T_{dq}}\mathbf{T}_{\alpha\mathbf{2}\beta\mathbf{2}}(\mathbf{M_{21}}-L_\Delta\mathbf{\Theta_{21}})\mathbf{T}^{-1}_{\alpha\mathbf{1}\beta\mathbf{1}}\mathbf{T}^{-1}_{\mathbf{dq}}\end{cases} \tag{7}$$

$$\begin{cases}T_{em}=\frac{3}{2}P\psi_{PM}(i_{q1}+i_{q2})\\ T_r=\frac{3}{2}P(L_{d1}-L_{q1})(i_{d1}i_{q1}+i_{d2}i_{q2})+\frac{3}{2}P(M_{d1d2}-M_{q1q2})(i_{d1}i_{q2}+i_{d2}i_{q1})\end{cases} \tag{15}$$

winding group can be expressed from (13)

$$T_e = \frac{3}{2}P(\psi_{PM} i_{q2} - 3L_\Delta i_{d2} i_{q2}). \tag{17}$$

If only one phase is opened, the other two healthy phases in the same winding group still can produce output torque. Without loss of generality, phase *a* is assumed to be opened and the currents for phase *abc* winding group are presented as

$$\mathbf{i_{abc}} = I_f \begin{bmatrix} 0 \\ \cos(\theta+\phi_1) \\ -\cos(\theta+\phi_1) \end{bmatrix} \tag{18}$$

where I_f is the amplitude of current when phase *a* is opened and ϕ_1 is the current angle for phase *abc*.

From the transformation, $d1q1$-axis currents are given by

$$\begin{bmatrix} i_{d1} \\ i_{q1} \end{bmatrix} = \mathbf{T_{dq}} \mathbf{T}_{\alpha\mathbf{1}\beta\mathbf{1}} \mathbf{i_{abc}} = \frac{\sqrt{3}I_f}{3} \begin{bmatrix} \sin(2\theta+\phi_1) - \sin\phi_1 \\ \cos(2\theta+\phi_1) + \cos\phi_1 \end{bmatrix}. \tag{19}$$

From (19), it can be seen that there are double-frequency current components of i_{d1} and i_{q1} which definitely contribute torque ripples. In order to mitigate the torque ripples, the compensation current components for the healthy three-phase winding should be 180° out of phase with the double-frequency components as shown in

$$\begin{aligned} i_{d2} &= -\frac{\sqrt{3}I_f}{3}\sin(2\theta+\phi_1) + I_{d20}, \\ i_{q2} &= -\frac{\sqrt{3}I_f}{3}\cos(2\theta+\phi_1) + I_{q20} \end{aligned} \tag{20}$$

where $I_{d20} = -I_0 \sin\phi_2$, $I_{q20} = I_0 \cos\phi_2$, I_0 is the current amplitude, and ϕ_2 is the current angle for phase *xyz*.

Based on (15), the double-frequency torque ripple is canceled off the steady torque produced by the rest five phases are expressed by

$$\begin{aligned} T_e = &\frac{3}{2}P\psi_{PM}\left(\frac{\sqrt{3}}{3}I_f\cos\phi_1 + I_0\cos\phi_2\right) + \frac{3}{4}PL_\Delta I_f^2 \sin 2\phi_1 \\ &+ \frac{9}{4}PL_\Delta I_0^2 \sin 2\phi_2 + \frac{3\sqrt{3}}{2}PL_\Delta I_f I_0 \sin(\phi_1+\phi_2). \end{aligned} \tag{21}$$

The torque modeling under single open-phase fault expressed in (21) is based on linear model of the inductances derived in (8) and (9). However, when the motor operates in the nonlinear saturated region, these inductances vary due to the magnetic saturation effect and the reluctance torque component of the torque model needs to be improved. The reluctance torque component under saturation situation can be expressed based on (15)

$$\begin{aligned} T_{r\_sat} &= \frac{3}{2}P(L_{d1} - L_{q1}) i_{d1} i_{q1} + \frac{3}{2}P(L_{d2} - L_{q2}) i_{d2} i_{q2} \\ &\quad + \frac{3}{2}P(M_{d1d2} - M_{q1q2})(i_{d1} i_{q2} + i_{d2} i_{q1}) \\ &= \frac{3}{2}P[l_{\Delta1} i_{d1} i_{q1} + l_{\Delta2} i_{d2} i_{q2} + m_\Delta(i_{d1} i_{q2} + i_{d2} i_{q1})] \end{aligned} \tag{22}$$

where $l_{\Delta1} = L_{d1} - L_{q1}, l_{\Delta2} = L_{d2} - L_{q2}$, and $m_\Delta = M_{d1d2} - M_{q1q2}$.

The steady reluctance torque components due to the dc current components of i_{d1}, i_{q1}, i_{d2}, and i_{q2} from (19) and (20) are

$$\begin{aligned} T_{r0\_}\text{sat} &= \frac{3}{2}P[l_{\Delta1} i_{d1} i_{q1} + l_{\Delta2} i_{d2} i_{q2} + m_\Delta(i_{d1} i_{q2} + i_{d2} i_{q1})] \\ &= \frac{3}{2}P\left[-\frac{I_f^2}{6}l_{\Delta1}\sin 2\phi_1 - I_0^2 l_{\Delta2} sin2\phi_2 \right. \\ &\quad \left. -\frac{\sqrt{3}I_f I_0}{3}m_\Delta \sin(\phi_1+\phi_2)\right]. \end{aligned} \tag{23}$$

The torque ripple caused by the double-frequency current components of i_{d1}, i_{q1}, i_{d2}, and i_{q2} from (19) and (20) can be expressed as

$$\begin{aligned} t_{r0\_\text{sat}} &= \frac{3}{2}P[l_{\Delta1} i_{d1} i_{q1} + l_{\Delta2} i_{d2} i_{q2} + m_\Delta(i_{d1} i_{q2} + i_{d2} i_{q1})] \\ &= \frac{3}{2}P\left[\frac{I_f^2}{6}l_{\Delta1}\sin 2(2\theta+\phi_1) + \frac{I_f^2}{6}l_{\Delta2} sin2(2\theta+\phi_1) \right. \\ &\quad \left. - \frac{I_f^2}{3}m_\Delta \sin 2(2\theta+\phi_1)\right] \\ &= \frac{PI_f^2 \sin(4\theta+2\phi_1)}{4}(l_{\Delta1} + l_{\Delta2} - 2m_\Delta). \end{aligned} \tag{24}$$

From (24), it shows that the double-frequency current components produce a quadruple-frequency torque component. In order to evaluate this torque ripple contributed by the magnetic saturation effect, finite element analysis is applied to calculated inductances under various operating conditions. Firstly, the inductance variations under healthy operation are examined under two different scenarios, namely current amplitude variation and current angle variation. Fig 2(a) and (b) shows the effects of the current amplitude and angle to the inductance differences $l_{\Delta1}$, $l_{\Delta2}$, and m_Δ, respectively. Term $l_{\Delta1}+l_{\Delta2}-2m_\Delta$ in (24) for cases (a) and (b) are shown in Fig. 2(c) and (d), respectively. Secondly, the inductance variations under a single open-phase fault operation are analyzed by keeping the current angles constant and changing the current amplitudes. Fig. 3(a)–(c) illustrates the variations of $l_{\Delta1}$, $l_{\Delta2}$, and m_Δ under these scenarios. Term $l_{\Delta1}+l_{\Delta2}-2m_\Delta$ for these three scenarios are calculated as shown in Fig. 3(d). Finally, the inductance variations under a single open-phase fault operation are analyzed by keeping the current amplitudes constant and changing the current angles. Fig. 4(a)–(c) illustrates the variations of $l_{\Delta1}$, $l_{\Delta2}$, and m_Δ under these scenarios. Term $l_{\Delta1}+l_{\Delta2}-2m_\Delta$ for these three scenarios are calculated as shown in Fig. 4(d). From Figs. 3–4, it is found that the amplitude variations of term $l_{\Delta1}+l_{\Delta2}-2m_\Delta$ are below 1 mH under single open-phase fault which are even lower than inductance variations under normal operation as shown in Fig. 2. When I_f and ϕ_1 are set to be its maximum value 15 A and 30°, respectively, the amplitude of torque ripple t_{r0_sat} is about 0.21 Nm which can be neglected compared to the developed steady torque. Therefore, the proposed torque modeling is also applicable in the nonlinear saturated region.

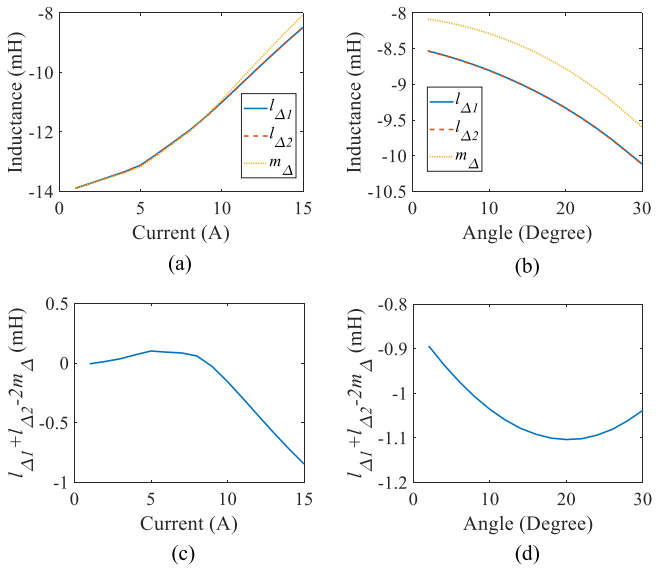

Fig. 2. Inductance variations under healthy operation. (a) Current amplitude I_0 variation. ($\phi_1 = \phi_2 = 0°$). (b) Current angle ϕ_1, ϕ_2 variation. ($\phi_1 = \phi_2$, I_0 = 15 A). (c) $l_{\Delta 1}$+$l_{\Delta 2}$–2m_Δ for case (a). (d) $l_{\Delta 1}$+$l_{\Delta 2}$–2m_Δ for case (b).

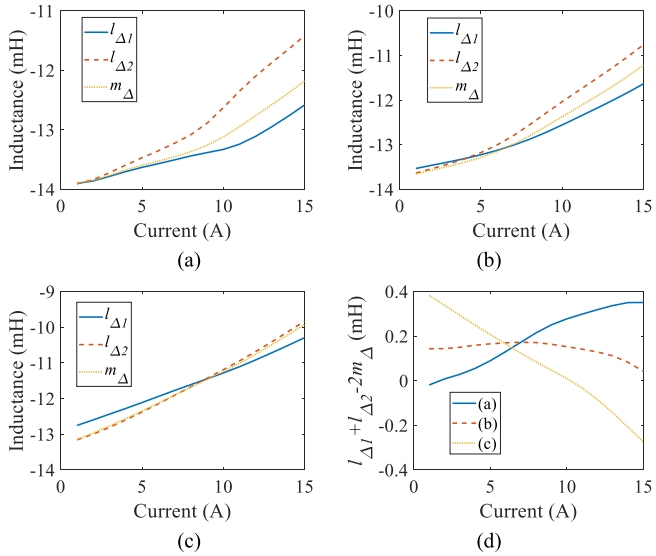

Fig. 3. Inductance variations under single open-phase fault operation. (a) Current amplitude I_0 variation. (I_f = 1 A, $\phi_1 = \phi_2 = 0°$). (b) Current amplitude I_0 variation. (I_f = 7 A, $\phi_1 = \phi_2 = 0°$). (c) Current amplitude I_0 variation. (I_f = 15 A, $\phi_1 = \phi_2 = 0°$). (d) $l_{\Delta 1}$+$l_{\Delta 2}$–2m_Δ.

IV. Fault-Tolerant Control With One Phase Opened

In order to control the faulty motor properly, the amplitudes and angles for currents flowing in the two winding groups should be controlled according to different operating targets, such as maximum torque and minimum losses [23]. Moreover, under faulty conditions, due to the compensated current will be injected into the healthy winding group, the currents will be asymmetrical and even excessive. Thus, the overcurrent protection should also be considered.

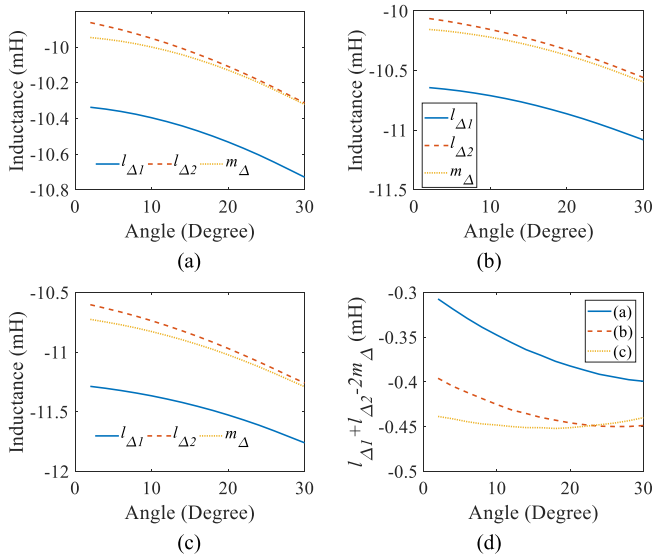

Fig. 4. Inductance variations under single open-phase fault operation. (a) Current angle ϕ_1 variation. ($I_0 = I_f$ = 15 A, ϕ_2 = 2). (b) Current angle ϕ_1 variation. ($I_0 = I_f$ = 15 A, ϕ_2 = 14). (c) Current angle ϕ_1 variation. ($I_0 = I_f$ = 15 A, ϕ_2 = 30). (d) $l_{\Delta 1}$+$l_{\Delta 2}$–2m_Δ.

A. Dual-Direction Rotating Reference Frames

To control the motor, the current reference signals should be calculated based on (19) and (20). However, from (19) and (20), it is observed that i_{d1}, i_{q1} and i_{d2}, i_{q2} both consist of a double-frequency current component and a dc component, respectively. The current control performance will be degraded with this current reference signals. The double-frequency component is caused by a negative current sequence which rotates in the same synchronous speed but the opposite direction. Therefore, in order to transform the double-frequency component into a dc component, another two *dq*-axis reference frames rotating clockwise are introduced, as shown in Fig. 5. The transformation matrix can be expressed as

$$\mathbf{T_{dq}}' = \begin{bmatrix} \cos\theta & -\sin\theta & 0 \\ \sin\theta & \cos\theta & 0 \\ 0 & 0 & 1 \end{bmatrix}. \tag{25}$$

By applying these two inverse transformations, the current for phase *abc* can be rewritten as the sum of a positive current sequence and a negative current sequence

$$\begin{aligned} \mathbf{i_{abc}} = & \frac{\sqrt{3}I_f}{3} \begin{bmatrix} \cos(\theta + \pi/2 + \phi_1) \\ \cos(\theta - \pi/6 + \phi_1) \\ -\cos(\theta + \pi/6 + \phi_1) \end{bmatrix} \\ & + \frac{\sqrt{3}I_f}{3} \begin{bmatrix} \cos(\theta - \pi/2 + \phi_1) \\ \cos(\theta + \pi/6 + \phi_1) \\ -\cos(\theta - \pi/6 + \phi_1) \end{bmatrix} \\ = & \mathbf{i_{abc\_1}} + \mathbf{i_{abc\_2}} = I_f \begin{bmatrix} 0 \\ \cos(\theta + \phi_1) \\ -\cos(\theta + \phi_1) \end{bmatrix}. \end{aligned} \tag{26}$$

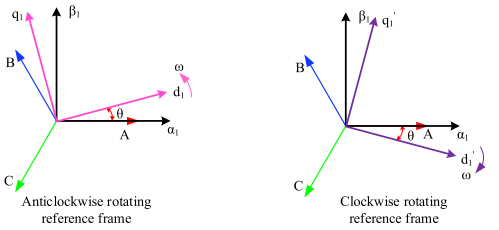

Fig. 5. Dual-direction rotating reference frame.

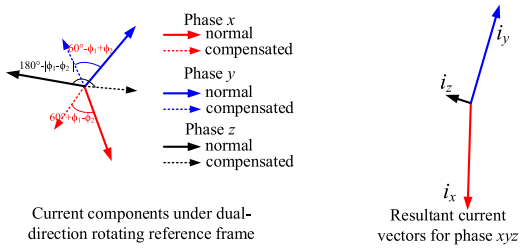

Fig. 6. Current vectors for phase *xyz* under open-phase fault.

Similarly, from (20), the current for phase *xyz* is

$$\mathbf{i_{xyz}} = I_0 \begin{bmatrix} \cos(\theta+\pi/3+\phi_2) \\ \cos(\theta-\pi/3+\phi_2) \\ -\cos(\theta+\phi_2) \end{bmatrix} + \frac{\sqrt{3}I_f}{3} \begin{bmatrix} \cos(\theta+2\pi/3+\phi_1) \\ \cos(\theta-2\pi/3+\phi_1) \\ \cos(\theta+\phi_1) \end{bmatrix}. \quad (27)$$

It can be found that the first term of the current is the one for normal operation which rotates anticlockwise and the second term of the current is to compensate the torque ripple producing by the faulty winding group which rotates clockwise.

Again, by using (5) and (25) for *dq* transformation, the currents under these dual *dq*-axis and dual-direction rotating reference frames can be expressed as

$$\begin{bmatrix} i_{d10} \\ i_{q10} \end{bmatrix} = \mathbf{T_{dq}} \mathbf{T}_{\alpha 1\beta 1} \mathbf{i_{abc\_1}} = \frac{\sqrt{3}I_f}{3} \begin{bmatrix} -\sin\phi_1 \\ \cos\phi_1 \end{bmatrix} \quad (28)$$

$$\begin{bmatrix} i_{d10}' \\ i_{q10}' \end{bmatrix} = \mathbf{T_{dq}}' \mathbf{T}_{\alpha 1\beta 1} \mathbf{i_{abc\_2}} = \frac{\sqrt{3}I_f}{3} \begin{bmatrix} \sin\phi_1 \\ \cos\phi_1 \end{bmatrix} \quad (29)$$

$$\begin{bmatrix} i_{d20} \\ i_{q20} \end{bmatrix} = I_0 \begin{bmatrix} -\sin\phi_2 \\ \cos\phi_2 \end{bmatrix}$$

$$\begin{bmatrix} i_{d20}' \\ i_{q20}' \end{bmatrix} = -\frac{\sqrt{3}I_f}{3} \begin{bmatrix} \sin\phi_1 \\ \cos\phi_1 \end{bmatrix}. \quad (30)$$

From the above equations, the currents for two winding groups are transformed into dc components and will be used for calculating the current reference signals to control the motor. The output torque can be calculated based on (15) with the currents i_{d10}, i_{q10} and i_{d20}, i_{q20}.

B. Overcurrent Protection

According to (27), the current vector diagram for phase *xyz* can be illustrated in Fig. 6. Hence, the current amplitude for each phase can be calculated as

$$\begin{cases} |i_x| = \sqrt{I_0^2 + I_f^2 \big/ 3 - 2\cos(2\pi/3 - \phi_1 + \phi_2) I_0 I_f / \sqrt{3}} \\ |i_y| = \sqrt{I_0^2 + I_f^2 \big/ 3 - 2\cos(2\pi/3 + \phi_1 - \phi_2) I_0 I_f / \sqrt{3}} \\ |i_z| = \sqrt{I_0^2 + I_f^2 \big/ 3 - 2\cos(|\phi_1 - \phi_2|) I_0 I_f / \sqrt{3}} \end{cases}. \quad (31)$$

The maximum current amplitude of phase *xyz* is

$$I_P = \sqrt{I_0^2 + I_f^2/3 - 2\cos(2\pi/3 + |\phi_1 - \phi_2|) I_0 I_f \big/ \sqrt{3}}. \quad (32)$$

In order to avoid overcurrent in the faulty operation, the maximum current amplitude should be constrained within reasonable operating conditions. According to (32), the current trajectories of I_f and I_0 for a given current constraint I_P is an ellipse. The allocation of I_f and I_0 definitely influences the FTC performance. Copper loss minimization and torque maximization are two main concerns selected to study the relationship between I_f and I_0. Apart from current amplitudes, current angles ϕ_1 and ϕ_2 are also required to be tuned to following the MTPA control under certain current amplitudes.

C. Copper Loss Maximization

During the fault-tolerant operation, the copper loss definitely increases due to the compensation current injection. The copper loss p_{cu1} and p_{cu2} for two winding groups are calculated as (33) shown at bottom of this page, where r_s is the phase resistance, and $\hat{i}_b$and $\hat{i}_c$are root-mean-square values of phases *b* and *c*.

The total average copper loss $\bar{p}_{cu}$ is

$$\bar{p}_{cu} = \bar{p}_{cu1} + \bar{p}_{cu2} = \frac{3}{2} r_s (I_f^2 + I_0^2) \quad (34)$$

where $\bar{p}_{cu1}$ and $\bar{p}_{cu2}$ are the average copper loss for phase *abc* and *xyz*, respectively.

In order to minimize the copper loss, the optimal current amplitudes I_f and I_0 and angles ϕ_1 and ϕ_2 should be determined

$$\begin{cases} p_{cu1} = r_s(\hat{i}_b^2 + \hat{i}_c^2) = r_s I_f^2 \\ p_{cu2} = \frac{3r_s}{2}(i_{d2}^2 + i_{q2}^2) = r_s[\frac{I_f^2}{2} + \frac{3I_0^2}{2} - \sqrt{3} I_0 I_f \cos(2\theta + \phi_1 + \phi_2)] \end{cases} \quad (33)$$

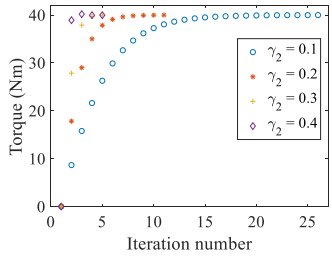

Fig. 7. Influence of step size γ_2 on convergence.

with the constraint of maximum current amplitude, (35) shown at bottom of this page.

By using the Lagrange multipliers to solve (35), the relationship between current amplitudes and angles of two winding groups should satisfy

$$(I_0^2 - I_f^2)\cos(2\pi/3 + |\phi_1 - \phi_2|) + 2I_0 I_f \Big/ \sqrt{3} = 0. \quad (36)$$

To find the optimal current amplitudes and angles for two phase winding groups to meet the target torque, two iteration loops are needed, namely angle iteration loop and amplitude iteration loop.

The gradient descent method is applied for angle loop iteration to obtain the optimal angles ϕ_1 and ϕ_2 for the MTPA control under a given current constraint I_P

$$(\phi_{1(n+1)}, \phi_{2(n+1)}) = (\phi_{1(n)}, \phi_{2(n)}) - \gamma_1\left(\frac{\partial T_e(\phi_{1(n)})}{\partial \phi_1}, \frac{\partial T_e(\phi_{2(n)})}{\partial \phi_2}\right) \quad (37)$$

where, in the unnumbered equation shown at the bottom of this page, the iteration stops when $|\phi_{1(n)} - \phi_{1(n-1)}| < \varepsilon$ and $|\phi_{2(n)} - \phi_{2(n-1)}| < \varepsilon$.

Since the current amplitudes between I_f and I_0 are governed by (36), the maximum current amplitude is updated steadily to meet the torque reference

$$I_{P(k+1)} = I_{P(k)} + \gamma_2(T_e^* - T_{e(k)}) \quad (38)$$

where the iteration stops when $|T_e^* - T_{e(k)}| < \varepsilon$.

Algorithm 1 gives the iteration process to find the optimal current amplitudes and angles to achieve the desired torque demand with minimized copper loss. Fig. 7 shows the convergence versus the step size γ_2, which shows that a suitable step size selection is essential for the search of optimal current amplitudes and angles.

Algorithm 1: FTC Algorithm For Copper Loss Minimization.

1. Initialize $I_{P(0)}$ for amplitude search, and $\phi_{1(0)}$ and $\phi_{2(0)}$ for angle search
2. Calculate $I_{0(0)}$, $I_{f(0)}$ with the initialized $\phi_{1(0)}$ and $\phi_{2(0)}$ based on (36)
3. Using (37), search for optimal angles
4. If $|\phi_{1(n)} - \phi_{2(n)}|$ is different from $|\phi_{1(n-1)} - \phi_{2(n-1)}|$, update the $I_{0(n+1)}$, $I_{f(n+1)}$; otherwise, calculate the output torque $T_{e(k)} = T_{e(n)}$
5. If $|T_e^* - T_{e(k)}| < \varepsilon$, iteration stops; otherwise, update $I_{p(k)}$ based on (38), and go to 2

D. Torque Maximization

It should be noted that for copper loss minimization, the current amplitudes between I_f and I_0 are governed by (36). For a given current amplitude constraint I_P, the maximum output torque point may not be searched. To achieve the maximum output torque for each given maximum current amplitude constraint, the optimal current amplitudes I_f and I_0 and angles ϕ_1 and ϕ_2 can be solved by

$$\begin{cases} \text{Maximize} \quad T_e\,, \quad \text{Minimize } I_P \\ \text{subject to } I_0^2 + I_f^2 \Big/ 3 - 2\cos(2\pi/3 + |\phi_1 - \phi_2|) I_0 I_f \Big/ \sqrt{3} \\ \qquad\qquad = I_P^2. \end{cases} \quad (39)$$

For each given current amplitude constraint I_P, in order to find out the optimal current amplitudes I_f and I_0 to maximize the output torque, a traversal algorithm is applied to update I_0

$$I_{0(m+1)} = I_{0(m)} + \gamma_3 \quad (40)$$

where γ_3 is the step size for traversal search of I_0, and the search stops once the maximum torque is obtained, namely $|T_{e(m)} - T_{e(m-1)}| < \varepsilon$.

Algorithm 2 gives the iteration process to find the optimal current amplitudes and angles to achieve the desired torque demand with minimum current constraint I_P. There are three iteration loops, namely angle loops for optimal angles ϕ_1 and ϕ_2, current amplitudes loop for the optimal current amplitudes I_f and I_0 for each given I_P, and current amplitude loop for finding the minimum current constraint I_P. Fig. 8 shows the convergence versus the step size γ_3. Due to the use of the traversal method for search of the optimal I_0, the iteration numbers are larger than that for the copper loss minimization. Therefore, for the

$$\begin{cases} Minimize \quad \bar{p}_{cu} = \frac{3}{2} r_s (I_f^2 + I_0^2) \\ \text{Subject to } I_0^2 + I_f^2 \Big/ 3 - 2\cos(2\pi/3 + |\phi_1 - \phi_2|) I_0 I_f \Big/ \sqrt{3} = I_P^2 \end{cases} \quad (35)$$

$$\begin{cases} \frac{\partial T_e}{\partial \phi_1} = -\frac{\sqrt{3}}{2} P \psi_{PM} I_f \sin\phi_1 \quad + \frac{3}{2} P L_\Delta I_f^2 \cos 2\phi_1 + \frac{3\sqrt{3}}{2} P L_\Delta I_f I_0 \cos(\phi_1 + \phi_2) \\ \frac{\partial T_e}{\partial \phi_2} = -\frac{3}{2} P \psi_{PM} I_0 \sin\phi_2 + \frac{9}{2} P L_\Delta I_0^2 \cos 2\phi_0 \quad + \frac{3\sqrt{3}}{2} P L_\Delta I_f I_0 \cos(\phi_1 + \phi_2) \end{cases}$$

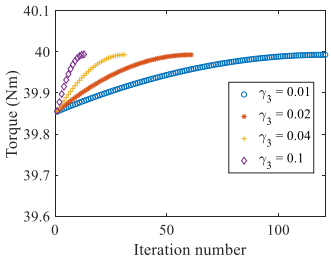

Fig. 8. Influence of step size γ_3 on convergence.

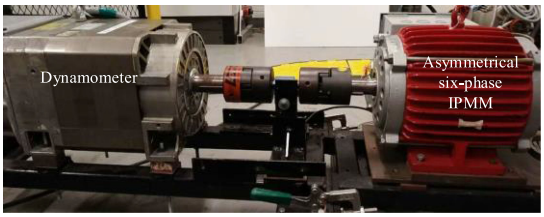

Fig. 9. Experimental test rig: asymmetrical six–phase IPMM and the dynamometer.

Algorithm 2: FTC Algorithm for Torque Maximization.

1. Initialize $I_{\mathrm{P}(0)}$ and $I_{0(0)}$ for amplitude search, and $\phi_{1(0)}$ and $\phi_{2(0)}$ for angle search
2. Calculate $I_{f(0)}$ with the initialized $\phi_{1(0)}$ and $\phi_{2(0)}$ based on the current amplitude constrain (33)
3. Using (37), search for optimal angles
4. If $|\phi_{1(\mathrm{n})} - \phi_{2(\mathrm{n})}|$ is different from $|\phi_{1(\mathrm{n}-1)} - \phi_{2(\mathrm{n}-1)}|$, update the $I_{0(\mathrm{n}+1)}$, $I_{f(\mathrm{n}+1)}$; otherwise, calculate the output torque $T_{e(\mathrm{m})} = T_{e(\mathrm{n})}$, $I_{0(\mathrm{m})} = I_{0(\mathrm{n})}$
5. If $|T_{e(\mathrm{m})} - T_{e(\mathrm{m}-1)}| < \varepsilon$, iteration stops and calculate output torque $T_{e(\mathrm{k})} = T_{e(\mathrm{m})}$; otherwise, update $I_{0(m+1)}$ using (40) and calculate $I_{f(\mathrm{m}+1)}$ using (32), and go to 3
6. If $|T_e^* - T_{e(\mathrm{k})}| < \varepsilon$, iteration stops; otherwise, update $I_{p(\mathrm{k})}$ based on (38), and go to 2

online search, the step size γ_3 should be appropriately selected to achieve a fast convergence with a relatively accurate solution.

V. Experimental Verification

To verify the proposed fault-tolerant control under four synchronous rotating frames, a test rig for an asymmetrical six-phase IPMM is implemented as shown in Fig. 9. The test system consists of two parallel voltage source inverters, a controller, and the investigated IPMM coupled to a dynamometer. These two inverters enable independent operation of the two three-phase winding groups. The main motor parameters are tabulated in Table I. Experimentation for four scenarios has been conducted to assess the proposed method. Scenarios 1, 2, and 3 are conducted for verifying the motor operating under the rated current condition with single-winding-group mode, FTC with copper loss minimization and FTC with torque maximization.

TABLE I
Specifications of Six-Phase IPMM

Parameters	Values
Rated power	4.5 kW
Rated current	15 A
Rated voltage	140 V
Rated torque	75 Nm
Rated speed	575 rpm
PM flux linkage	0.337 Wb–turn
Stator resistance	0.73 Ω
Number of PM pole–pairs	4

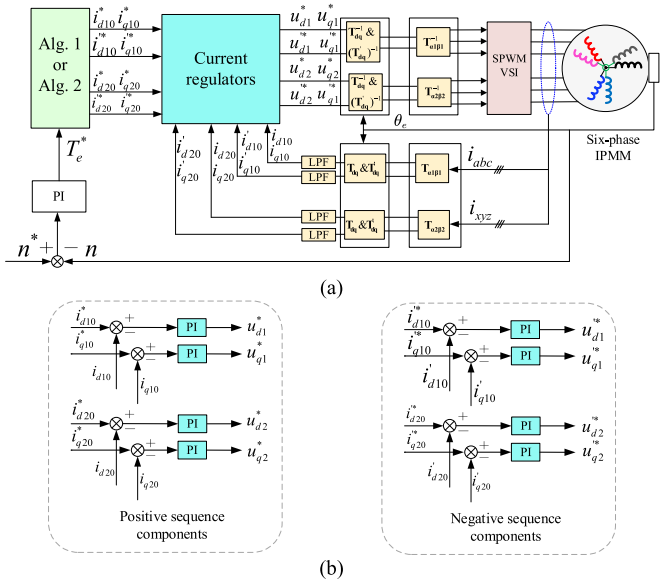

Fig. 10. Implementation of the proposed FTC. (a) Control block diagram for the asymmetrical six–phase IPMM drive based on dual synchronous rotating frames. (b) Current regulators for positive and negative sequence current components.

Scenario 4 is carried out for testing the transitions with a constant output torque between the healthy mode and the other three fault–tolerant operating modes. Moreover, the dynamic analysis and comparison with other FTC method are also performed to verify the proposed modeling and FTC method.

The implementation of the proposed FTC is shown in Fig. 10. Both current and speed control loops are applied with the regular proportional-integral (PI) controllers for four rotating reference frames. As shown in Fig. 10(a), by using the dual-direction rotating reference frame, the current in each rotating reference frame is transformed into dc and double-frequency components as defined in (19) and (20). In order to mitigate the double-frequency perturbation, the low-pass filters are applied to obtain the exact dc components for each synchronous rotating reference frame. Then, eight PI current controllers are applied to regulate these dc components of both positive and negative sequence components, as shown in Fig. 10(b). The dc reference signals are calculated based on the torque reference signals and the selected algorithm. Due to the symmetry of the magnetic structure, the equivalent circuits for the anticlockwise rotating frame are identical to those of the clockwise rotating frame.

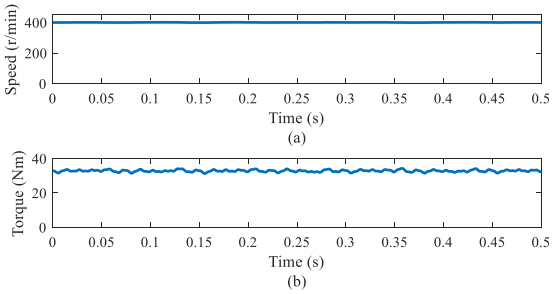

Fig. 11. Measured waveforms of single-winding-group operation. (a) Speed. (b) Torque.

The PI parameters are determined using the same method for the normal condition. By using the pole-placement method to design the PI controllers, the stability of these controllers is guaranteed. Since the time constants for the current loop and speed loop are different, which are about 20–30 ms for the current loop and over 100 ms for the speed loop, respectively. The cutoff frequencies are set as 1000 rad/s for PI controllers in the current loop and 100 rad/s for the speed loop. The damping factors are set as 0.707 for all current and speed PI controllers. The PI coefficients are calculated based on the relevant motor parameters, cutoff frequencies, and damping factors. The step sizes for γ_2 and γ_3 are selected as 0.4 and 0.1 in the implemented algorithm as shown in Fig. 7.

A. Single-Winding-Group Operation

Firstly, the winding group *abc* is de-energized from the inverter due to the open-phase fault of phase *a* and only winding group *xyz* is in operation. In this scenario, the current amplitude constraint I_P is kept at 15 A and motor operating speed is set at 400 r/min. The measured speed, torque, and current waveforms are shown in Figs. 11 and 12, respectively. Under this situation, the average torque is about 32.8 Nm, the torque ripple is about 9.03%, and the average copper loss is 246.38 W. When there are more than one phase in the winding group *abc* opened, this operating mode can still be implemented. The dual *dq*-axis currents only have the dc components.

B. FTC With Copper Loss Minimization

Secondly, the condition of the current amplitude constraint and operating speed is the same as scenario 1. Therefore, the iteration for searching I_P in Algorithm 1 is not required. By gradient descent method, the search of the optimal angles and then updated the current amplitudes for I_f and I_0 is conducted to minimize the copper loss. The optimal current amplitudes for I_f and I_0 and the optimal angles for ϕ_1 and ϕ_2 are 4.96 A, 13.36 A, 21.91°, and 21.91°, respectively. The measured speed, torque, and current waveforms are shown in Figs. 13 and 14, respectively. Under this situation, the average torque is 36.1 Nm, the torque ripple is about 9.26%, and the copper loss is 222.38 W. Compared with the single-winding-group mode, the output torque is improved by 9.14%, and copper loss is reduced by 9.74%. As shown in Fig. 11(c)–(f), current waveforms for i_{d1}, i_{q1}, i_{d2}, i_{q2}, i_{d1}', i_{q1}', i_{d2}', and i_{q2}' have both the dc components and the ac components. The amplitude of the dc components coincides with the values calculated by (28), (29), and (30). It means that the compensated currents in phase *xyz* work well to cancel off the negative current sequence in phase *abc* due to the open-phase fault and the torque ripple-free operation is achieved. It confirms the validity of the proposed multireference open-phase fault model.

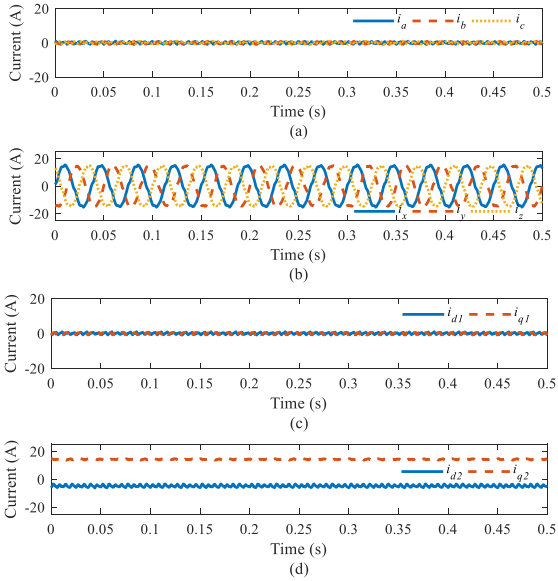

Fig. 12. Measured current waveforms of single-winding-group operation. (a) i_{abc}. (b) i_{xyz}. (c) i_{d1} and i_{q1}. (d) i_{d2} and i_{q2}.

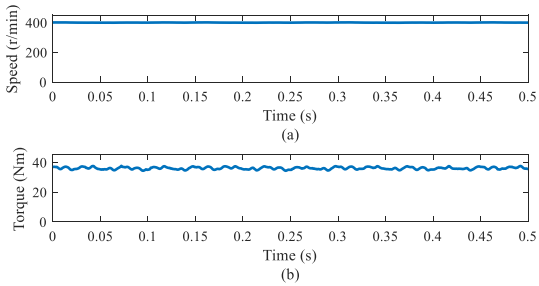

Fig. 13. Measured waveforms of proposed FTC with copper loss minimization. (a) Speed. (b) Torque.

C. FTC With Torque Maximization

Thirdly, the condition of the current amplitude constraint and operating speed is the same as scenario 1. This test aims to maximize motor output torque with the same current amplitude constraint $I_P = 15$ A. Again, the iteration for searching I_P in Algorithm 2 is not required. The gradient descent method is applied to search for optimal angles ϕ_1 and ϕ_2, and the traversal method is used to search for the optimal current amplitudes I_f and I_0 to maximize the output torque. The optimal current amplitudes for I_f and I_0 and the optimal angles for ϕ_1 and ϕ_2 are 13.7 A, 9.39 A, 23.09°, and 23.09°, respectively. The measured speed, torque, and current waveforms are shown in Figs. 15 and 16,

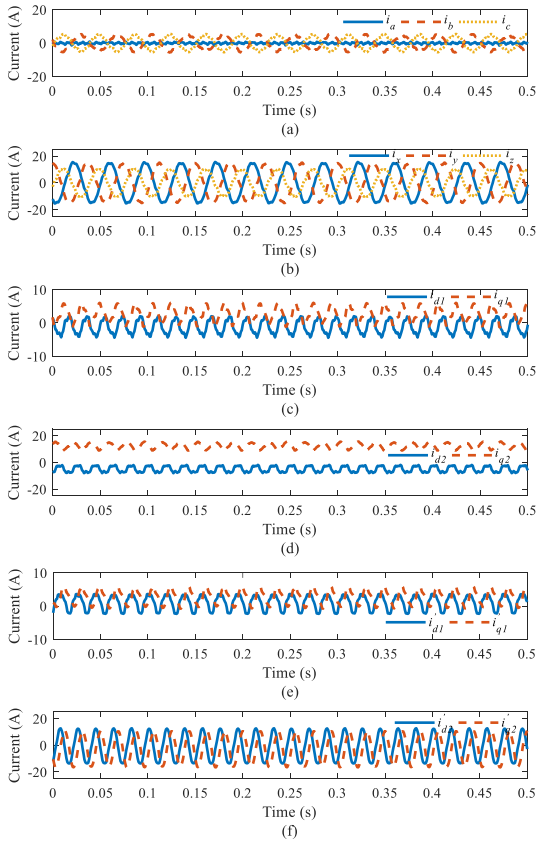

Fig. 14. Measured waveforms of proposed FTC with copper loss minimization. (a) i_{abc}. (b) i_{xyz}. (c) i_{d1} and i_{q1}. (d) i_{d2} and i_{q2}. (e) $i^{'}{}_{d1}$ and $i^{'}{}_{q1}$. (f) $i^{'}{}_{d2}$ and $i^{'}{}_{q2}$.

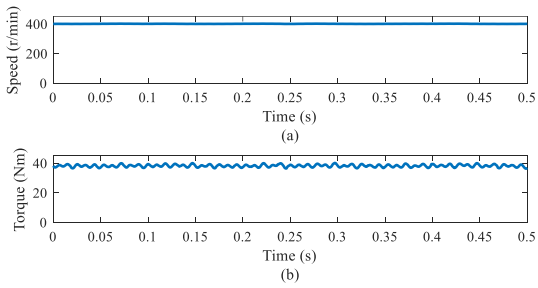

Fig. 15. Measured waveforms of proposed FTC with torque maximization. (a) Speed. (b) Torque.

respectively. Under this FTC mode, the average torque is 38.8 Nm and the torque ripple is about 10.2%.

The output torque and copper loss under three FTC schemes are compared in Fig. 17. At the same current amplitude, compared with the single-winding-group mode, the torque is improved by 18.3% and copper loss increases by 22.6% for the torque maximization mode, while the torque is improved by 10.1% and the copper loss decreases by 9.7% for the copper loss minimization mode which verifies the effectiveness of the proposed FTC schemes.

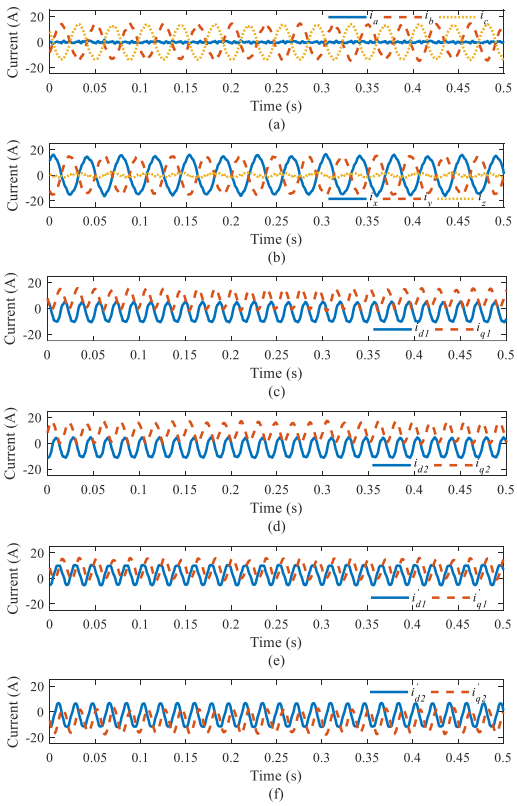

Fig. 16. Measured waveforms of proposed FTC with torque maximization. (a) i_{abc}. (b) i_{xyz}. (c) i_{d1} and i_{q1}. (d) i_{d2} and i_{q2}. (e) $i^{'}{}_{d1}$ and $i^{'}{}_{q1}$. (f) $i^{'}{}_{d2}$ and $i^{'}{}_{q2}$.

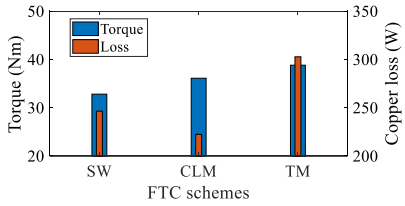

Fig. 17. Torque and loss under different FTC schemes (SW: single–winding–group operation; CLM: copper loss minimization mode; TM: torque maximization mode).

D. Transition Between FTC Schemes

In this test, the operating speed is set to 350 r/min, and the reference torque is set to 28 Nm. Four operating stages, namely healthy operation—Stage I (0–5 s); single-winding-group operation—Stage II (5–10 s); FTC operation with copper loss minimization—Stage III (10–15 s); and FTC operation with torque maximization—Stage IV (15–20 s), run one by one. The measured speed and torque waveforms are shown in Fig. 18, and the current waveforms between transitions of each stage are shown in Fig. 19. It was found that the speed and torque are maintained at 350 r/min and 28 Nm. When the motor runs in healthy mode, the current amplitude for both winding groups is 6.48 A, the torque ripple is 10.4%, and the average copper loss is 91.96 W. Fig. 20 compares the torque and copper loss under these four operation scenarios. Compared to the healthy operation,

TABLE II
OPERATING FACTS UNDER DIFFERENT STAGES

Control method	Stage I Healthy	Stage II Phase *xyz* in operation	Stage III Copper loss minimization	Stage IV Torque maximization
I_f (A)	–	0	4.0	10.95
I_0 (A)	6.48	13.07	10.67	6.75
I_P (A)	6.48	13.07	12.0	11.32
ϕ_1 (°)	19.0	–	19.01	19.11
ϕ_2 (°)	19.0	19.0	19.01	19.11
Torque (Nm)	28	28	28	28
Torque ripple	10.4%	13.2%	11.6%	16.6%

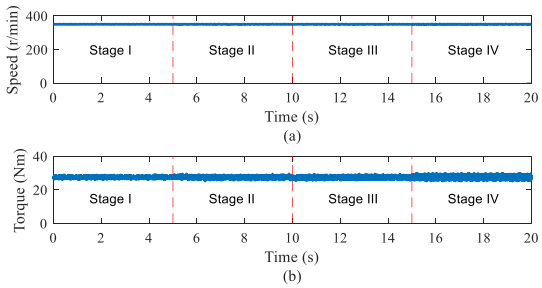

Fig. 18. Measured waveforms of proposed control under transient state. (a) Speed. (b) Torque.

the copper losses increase by 103.4%, 54.8%, and 97.1% for the single-winding-group operation, copper loss minimization mode, and torque maximization mode, respectively. It shows that using the FTC with copper loss minimization, the copper loss is suppressed significantly.

The operating facts for the other three modes are shown in Table II. It can be observed that with copper loss minimization, the torque ripple (11.6%), and the copper loss (142.42 W) are the lowest among three FTC operating modes, while the torque ripple is largest with torque maximization, and copper loss is highest with single-winding-group mode. Apart from the healthy mode, the current amplitude is 11.32 A for the torque maximization mode which is the lowest, while the highest current amplitude is 13.07 A for the single-winding-group mode. It should also be noted that during the transition between each stage, no spikes occur in neither the speed nor the torque waveforms which shows that the control performance is robust based on the proposed dual *dq*-axis dual-direction rotating reference frames.

E. Dynamic Performance Analysis

To evaluate the dynamic performance of the proposed fault modeling and control algorithm, the load torque step and speed step responses are carried out for the proposed FTC under modes of copper loss minimization and torque maximization to test the performances for both the current loop and speed loop of the controllers. Firstly, the current loop control is evaluated for both copper loss minimization and torque maximization modes. The torque and speed steps are applied when the investigated IPMM is in current loop control. The torque and speed step

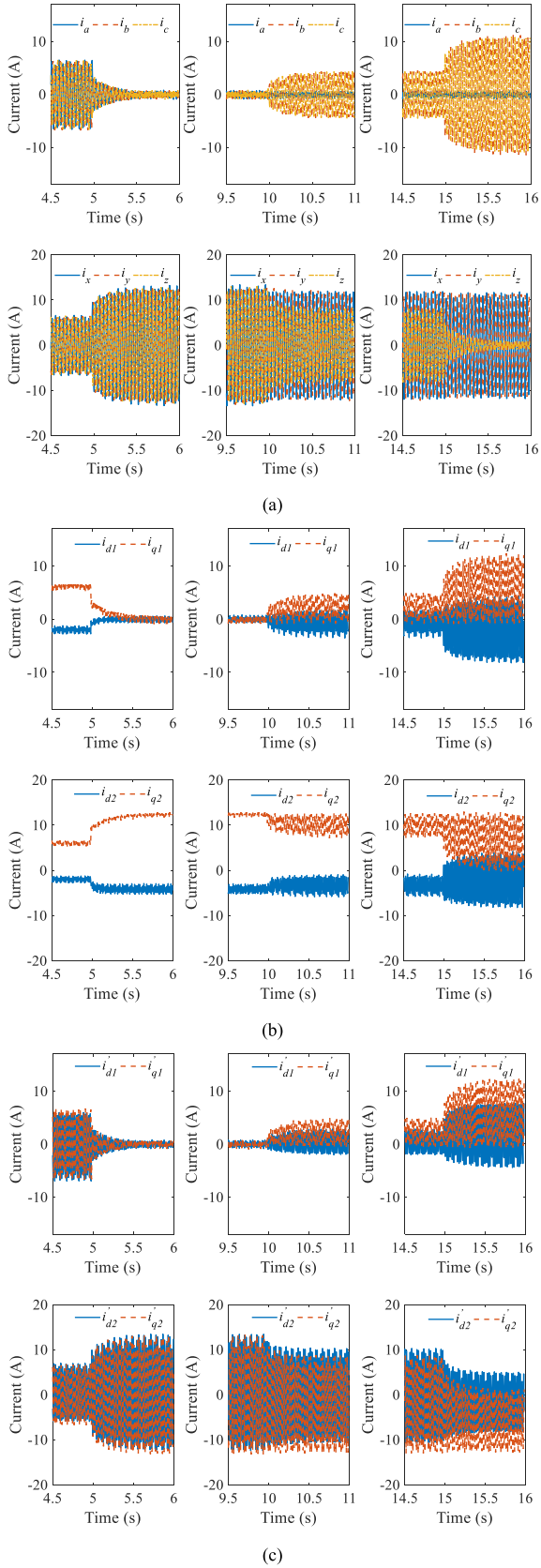

Fig. 19. Measured current waveforms of proposed control under transient state. (a) i_{abc}. and i_{xyz}. (b) i_{d1}, i_{q1}, i_{d2}, and i_{q2}. (c) $i^{'}_{d1}$, $i^{'}_{q1}$, $i^{'}_{d2}$, and $i^{'}_{q2}$.

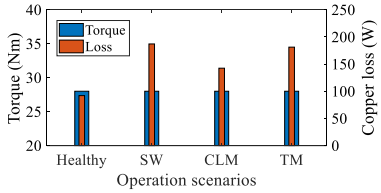

Fig. 20. Torque and copper losses under different operation scenarios (SW: single-winding-group operation; CLM: copper loss minimization mode; TM: torque maximization mode).

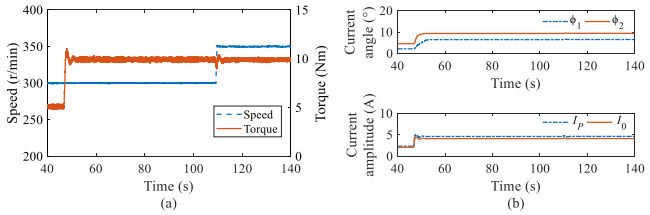

Fig. 21. Torque and speed step responses for current loop control under copper loss minimization mode. (a) Torque and speed curves. (b) Current angle and amplitude iteration processes.

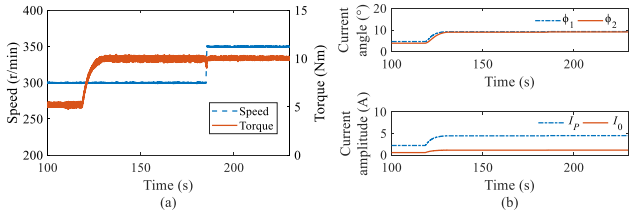

Fig. 22. Torque and speed step responses for current loop control under torque maximization mode. (a) Torque and speed curves. (b) Current angle and amplitude iteration processes.

responses and current angle and amplitude iteration processes under copper loss minimization mode are shown in Fig. 21. The motor runs at 300 r/min while the torque step from 5 to 10 Nm is applied to the drive system at around 47 s. It shows that the motor can trace the torque step fast and both the iterations for current angles and amplitudes converge quickly. Then, the motor output torque maintains at 10 Nm while the speed changes from 300 to 350 r/min applied to the drive system at around 109 s. The motor torque drops 5% during the speed transition, and the speed disturber affects slightly the iterations for current angles and amplitudes.

Similarly, the torque and speed steps are applied to the drive system under the torque maximization mode to verify the current loop control performance. The torque and speed step responses and current angle and amplitude iteration processes under torque maximization mode are shown in Fig. 22. The motor runs at 300 r/min while the torque step from 5 to 10 Nm is applied to the drive system at around 118 s. The motor can trace the torque step fast and both the iterations for current angles and amplitudes converge quickly. But compared with the FTC under copper loss minimization mode, the transient is longer. The motor output torque keeps at 10 Nm while the speed changes from 300 to 350 r/min applied to the drive system at around 185 s. It shows

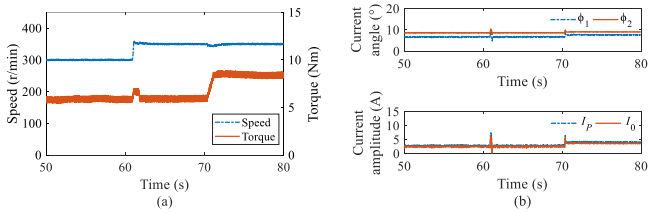

Fig. 23. Speed and load torque step responses for speed loop control under copper loss minimization mode. (a) Torque and speed curves. (b) Current angle and amplitude iteration processes.

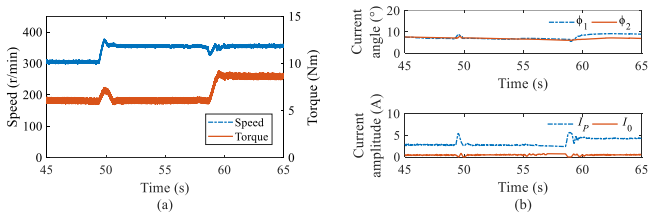

Fig. 24. Speed and load torque step responses for speed loop control under torque maximization mode. (a) Torque and speed curves. (b) Current angle and amplitude iteration processes.

that the speed disturber affects slightly the iterations for current angles and amplitudes under current loop control. Compared with the FTC under the copper loss minimization mode, the current amplitude I_P is smaller and ϕ_1 is greater than ϕ_2 under this operating mode.

The speed loop control for the investigated IPMM is also assessed under similar scenarios. The speed and load torque steps are applied to the system using the proposed FTC under modes of copper loss minimization and torque maximization. The speed and load torque step responses and current angle and amplitude iteration processes under copper loss minimization mode are shown in Fig. 23. A speed step reference signal from 300 to 350 r/min is applied to the drive system at around 61 s while the load torque is about 5.9 Nm. The transition for the speed controller can trace the speed step fast and both the iterations for current angles and amplitudes converge quickly. Then, the motor speed keeps at 350 r/min while the load torque changes from 5.9 to 8.5 Nm applied to the drive system at around 70 s. It shows that the motor speed drops 2.8% during the torque transition and the settling time is about 1.5 s.

The speed and load torque step responses and current angle and amplitude iteration processes under torque maximization mode for the speed loop control are shown in Fig. 24. A speed step reference signal from 300 to 350 r/min is applied to the drive system at around 50 s while the load torque is about 5.9 Nm. Compared to Fig. 23, the motor can trace the speed step at a slower pace and both the iterations for current angles and amplitudes converge for a longer time. Then, the motor speed keeps at 350 r/min while the load torque changes from 5.9 to 8.7 Nm applied to the drive system at around 58 s. The motor speed drops 5.7% at the torque transition and the transition takes about 2 s for the speed to settle down. Compared with the FTC under copper loss minimization mode, the torque ripple is larger

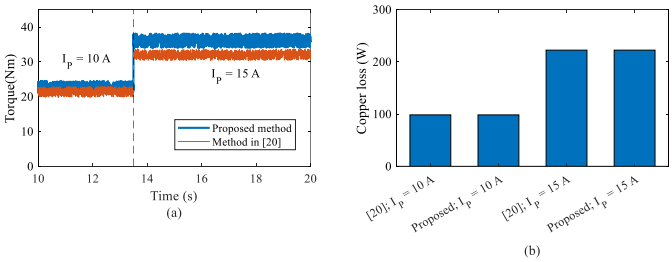

Fig. 25. Comparison under copper loss minimization mode. (a) Torque curves. (b) Copper losses.

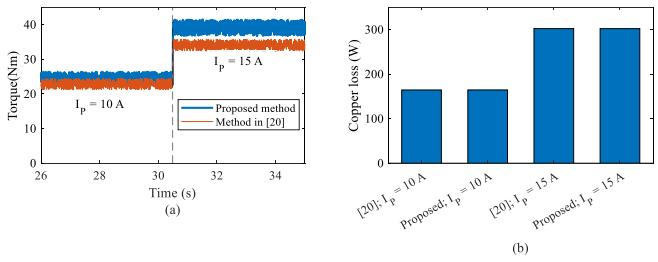

Fig. 26. Comparison under torque maximization mode. (a) Torque curves. (b) Copper losses.

and the convergence time is longer for torque maximization mode. It is due to the current amplitude searching algorithm is time-consuming for torque maximization. Current amplitudes I_P for the same output torque are 4.27 and 4.18 A under modes of copper loss minimization and torque maximization which confirm that the current amplitude is lower under the torque maximization mode.

F. Performance Comparison

In order to further evaluate the proposed model and FTC algorithm, a comparison is performed with the method proposed in [20] which deals with the open-phase fault for dual three-phase surface-mounted PMSM. In [20], the dual three-phase PMSM is also divided into two winding groups (PMSM-1 and PMSM-2) with two independent neutral points. The torque model in [20] is also the sum of torque components from two winding groups. Both copper loss minimization mode and torque maximization mode are studied and compared. To make a fair comparison, the current limits are imposed on the operation for both methods. To protect overcurrent, the maximum current amplitudes I_P are set for 10 and 15 A, respectively. Firstly, methods for the copper loss minimization mode are compared and the torque waveforms and copper losses are shown in Fig. 25. When I_P is 10 A, the average torque is 22.7 and 21.3 Nm for the proposed method and the compared method. When I_P is 15 A, the average torque is 36.1 and 32.1 Nm for the proposed method and the compared method. The copper losses are approximately 98.5 and 222.4 W for both methods with current limits of 10 and 15 A, respectively. It is found that with the proposed method that utilizes the reluctance torque, the torque is improved 6.6% and 12.5% for 10 A and 15 A, respectively.

Investigations are performed for the same operating conditions under the torque maximization mode. Fig. 26 shows the torque waveforms and copper losses for the two methods. When I_P is 10 A, the average torque is 24.5 and 22.8 Nm for the proposed method and the compared method. When I_P is 15 A, the average torque is 38.8 and 33.7 Nm for the proposed method and the compared method, respectively. The copper losses are approximately 164.4 and 302.1 W for both methods under 10 and 15 A, respectively. It is observed that with the proposed method, the torque is improved 7.5% and 15.1% for 10 and 15 A, respectively. The comparison shows that under the same copper losses, the proposed method can contribute 15% more torque by utilizing the reluctance torque which confirms the validity of the proposed method.

VI. Conclusion

In this article, a multireference frame based fault-tolerant modeling and control for an asymmetrical six-phase IPMM under open-phase fault are proposed and verified by experimentation. By using the four synchronous rotating frames, mathematical models considering the magnetic saturation effect for the phase currents and torque under a single open-phase fault are established. The copper loss and output torque as two main objectives are adopted for fault-tolerant control algorithm design and the maximum current amplitude is selected as the constraint with consideration of overcurrent protection. The experiments are carried out in different scenarios to verify steady and dynamic performances of the proposed open-phase fault modeling and control. The results demonstrate that with the proposed FTC strategy, the motor can run properly under different operating modes. Under the same current amplitude, the algorithm for torque maximization can output a higher torque, while under the same reference torque, the algorithm for copper loss minimization can exhibit a lower torque ripple and less copper loss compared to the other two FTC schemes.

References

[1] K. Wang *et al.*, "Torque improvement of dual three–phase permanent–magnet machine with third–harmonic current injection," *IEEE Trans. Ind. Electron.*, vol. 62, no. 11, pp. 6833–6844, Nov. 2015.

[2] P. Xu et al.*et al.*, "Analysis of dual three–phase permanent–magnet synchronous machines with different angle displacements," *IEEE Trans. Ind. Electron.*, vol. 65, no. 3, pp. 1941–1954, Mar. 2018.

[3] Y. Demir and M. Aydin, "A novel dual three-phase permanent magnet synchronous motor with asymmetric stator winding," *IEEE Trans. Magn.*, vol. 52, no. 7, pp. 1–5, Jul. 2016.

[4] M. Barcaro, N. Bianchi, and F. Magnussen, "Analysis and tests of a dual three-phase 12-slot 10-pole permanent-magnet motor," *IEEE Trans. Ind. Appl.*, vol. 46, no. 6, pp. 2355–2362, Nov./Dec. 2010.

[5] X. Wang *et al.*, "Comprehensive diagnosis and tolerance strategies for electrical faults and sensor faults in dual three-phase PMSM drives," *IEEE Trans. Power Electron.*, vol. 34, no. 7, pp. 6669–6684, Jul. 2019.

[6] H. M. Eldeeb, A. S. Abdel-Khalik, and C. M. Hackl, "Postfault full torque–speed exploitation of dual three-phase IPMSM drives," *IEEE Trans. Ind. Electron.*, vol. 66, no. 9, pp. 6746–6756, Sep. 2019.

[7] D. Ye et al.*et al.*, "Study on steady-state errors for asymmetrical six-phase permanent magnet synchronous machine fault-tolerant predictive current control," *IEEE Trans. Power Electron.*, vol. 35, no. 1, Jan. 2020, pp. 640–651.

[8] Z. Wang, X. Wang, M. Cheng, and Y. Hu, "Comprehensive investigation on remedial operation of switch faults for dual three-phase PMSM drives fed by T-3L inverters," *IEEE Trans. Ind. Electron.*, vol. 65, no. 6, pp. 4575–4587, Jun. 2018.
[9] F. Barrero et al.*et al.*, "A proof of concept study of predictive current control for VSI-driven asymmetrical dual three-phase AC machines," *IEEE Trans. Ind. Electron.*, vol. 56, no. 6, pp. 1937–1954, Jun. 2009.
[10] Y. Zhao and T. A. Lipo, "Space vector PWM control of dual three-phase induction machine using vector space decomposition," *IEEE Trans. Ind. Appl.*, vol. 31, no. 5, pp. 1100–1109, Sep./Oct. 1995.
[11] Y. Hu, Z. Q. Zhu, and M. Odavic, "Comparison of two-individual current control and vector space decomposition control for dual three-phase PMSM," *IEEE Trans. Ind. Appl.*, vol. 53, no. 5, pp. 4483–4492, Sep. 2017.
[12] J. Karttunen *et al.*, "Decoupled vector control scheme for dual three-phase permanent magnet synchronous machines," *IEEE Trans. Ind. Electron.*, vol. 61, no. 5, pp. 2185–2196, May 2014.
[13] M. L. Woldesemayat, H. Lee, S. Won, and K. Nam, "Modeling and verification of six–phase interior permanent magnet synchronous motor," *IEEE Trans. Power Electron.*, vol. 33, no. 10, pp. 8661–8671, Oct. 2018.
[14] A. Arafat, S. Choi, and J. Baek, "Open-phase fault detection of a five-phase permanent magnet assisted synchronous reluctance motor based on symmetrical components theory," *IEEE Trans. Ind. Electron.*, vol. 64, no. 8, pp. 6465–6474, Aug. 2017.
[15] M. Bermudez, I. Gonzalez-Prieto, F. Barrero, H. Guzman, M. J. Duran, and X. Kestelyn, "Open-phase fault-tolerant direct torque control technique for five-phase induction motor drives," *IEEE Trans. Ind. Electron.*, vol. 64, no. 2, pp. 902–911, Feb. 2017.
[16] F. Yu, M. Cheng, and K. T. Chau, "Controllability and performance of a nine-phase FSPM motor under severe five open-phase fault conditions," *IEEE Trans. Energy Convers.*, vol. 31, no. 1, pp. 323–332, Mar. 2016.
[17] Y. Zhou, X. Lin, and M. Cheng, "A fault-tolerant direct torque control for six-phase permanent magnet synchronous motor with arbitrary two opened phases based on modified variables," *IEEE Trans. Energy Convers.*, vol. 31, no. 2, pp. 549–556, Jun. 2016.
[18] I. González–Prieto, M. J. Duran, and F. J. Barrero, "Fault-tolerant control of six-phase induction motor drives with variable current injection," *IEEE Trans. Power Electron.*, vol. 32, no. 10, pp. 7894–7903, Oct. 2017.
[19] M. J. Duran *et al.*, "Optimal fault-tolerant control of six-phase induction motor drives with parallel converters," *IEEE Trans. Ind. Electron.*, vol. 63, no. 1, pp. 629–640, Jan. 2016.
[20] W. Wang *et al.*, "Fault-tolerant control of dual three-phase permanent-magnet synchronous machine drives under open-phase faults," *IEEE Trans. Power Electron.*, vol. 32, no. 3, pp. 2052–2063, Mar. 2017.
[21] G. Feng, C. Lai, W. Li, J. Tjong, and N. C. Kar, "Open-phase fault modeling and optimized fault tolerant control of dual three-phase permanent magnet synchronous machines," *IEEE Trans. Power Electron.*, vol. 34, no. 11, pp. 11116–11127, Nov. 2019.
[22] B. Lu and S. K. Sharma, "A literature review of IGBT fault diagnostic and protection methods for power inverters," *IEEE Trans. Ind. Appl.*, vol. 45, no. 5, pp. 1770–1777, Sep./Oct. 2009.
[23] F. Baneira, J. Doval-Gandoy, A. G. Yepes, Ó. López, and D. Pérez-Estévez, "Control strategy for multiphase drives with minimum losses in the full torque operation range under single open-phase fault," *IEEE Trans. Power Electron.*, vol. 32, no. 8, pp. 6275–6285, Aug. 2017.

Wenlong Li (Senior Member, IEEE) received the B.Eng. degree from Sichuan University, Chengdu, China, in 2005, the M.Eng. degree from the University of Science and Technology of China, Hefei, China, in 2008, and the Ph.D. degree from the University of Hong Kong, Hong Kong, China, in 2012.

He was a Visiting Scholar at the University of Windsor, Windsor, ON, Canada, from 2018 to 2021. He is currently with the School of Automation, Nanjing University of Science and Technology, Nanjing, China. His research interests include electrical machine design, analysis and applications, with special interests for the areas of renewable energy systems and electromobility. He has authored or coauthored more than 70 peer-viewed technical papers and three invited book chapters in these areas.

Guodong Feng (Senior Member, IEEE) received the B.S. and Ph.D. degrees in engineering from the School of Information, Science and Technology, Sun Yat-sen University, Guangzhou, China, in 2010 and 2015, respectively.

From 2015 to 2019, he worked as a Postdoctoral Fellow with the University of Windsor, Windsor, ON, Canada. He is currently an Associate Professor with the School of Intelligent Systems Engineering, Sun Yat-sen University, Guangzhou, China. His research interests include advanced signal processing, optimization, and electrical machines and drives.

Ze Li (Student Member, IEEE) received the B.Eng. and M.Eng. degrees from the Xi'an University of Architecture and Technology, Xi'an, China, in 2012 and 2015, respectively. He is currently working toward the Ph.D. degree with the University of Windsor, Windsor, ON, Canada.

He worked as Testing Engineer with D&V Electronics Co., Ltd., Shanghai, China, in 2017. His research interests include modeling and control of electric power converters and electrical machines and machine parameter identification, testing, and performance analysis.

Jimi Tjong received the B.Sc., M.Sc., and Ph.D. degrees in mechanical engineering from the University of Windsor, Windsor, ON, Canada, in 1980, 1984, and 1993, respectively.

He is currently an Adjunct Professor with the University of Windsor, the University of Toronto, Toronto, ON, and McMaster University, Hamilton, ON, Canada. His research interests include production and comprehensive design validation of components and systems for conventional and electrified vehicles and optimization of automotive test systems for cost, performance, and compatibility.

Narayan C. Kar (Senior Member, IEEE) received the B.Sc. degree from the Bangladesh University of Engineering and Technology, Dhaka, Bangladesh, in 1992, and the M.Sc. and Ph.D. degrees from Kitami Institute of Technology, Hokkaido, Japan, in 1997 and 2000, respectively, all in electrical engineering.

He is currently a Professor with the Electrical and Computer Engineering Department, University of Windsor, ON, Canada. He is also the Director of the Centre for Hybrid Automotive Research and Green Energy (CHARGE), University of Windsor. His research interests include the analysis, design, and control of electrical machines for electrified vehicle applications; and testing and performance analysis of batteries and optimization techniques for hybrid energy management system.